Journal of ELECTRONIC MATERIALS, Vol. 42, No. 7, 2013
DOI: 10.1007/s11664-012-2406-x

New Perspectives in Thermoelectric Energy Recovery System Design Optimization

TERRY J. HENDRICKS,[1,5] NAVEEN K. KARRI,[2] TIM P. HOGAN,[3] and CHARLES J. CAUCHY[4]

1.—Battelle Memorial Institute, Columbus, OH 43201, USA. 2.—Pacific Northwest National Laboratory, Richland, WA 99352, USA. 3.—Electrical & Computer Engineering Department, Michigan State University, East Lansing, MI 48824, USA. 4.—Promethient, LLC, Traverse City, MI 49686, USA. 5.—e-mail: hendrickst@battelle.org

It is highly desirable to develop technologies that recover the large amounts of waste heat generated worldwide in industrial processes, automotive transportation, diesel engine exhaust, military generators, and incinerators to increase fuel efficiency and reduce CO_2 production and the environmental footprint of these applications. Recent work has investigated new thermoelectric (TE) materials and systems that can operate at higher performance levels and show a viable pathway to lightweight, small-form-factor, advanced thermoelectric generator (TEG) systems to recover waste heat in many of these applications. New TE materials include nanocomposite materials such as lead-antimony-silver-telluride (LAST) and lead-antimony-silver-tin-telluride (LASTT) compounds. These new materials have created opportunities for high-performance, segmented-element TE devices. New higher-performance TE devices segmenting LAST/LASTT materials with bismuth telluride have been designed and fabricated. Sectioned TEG systems using these new TE devices and materials have been designed. Integrated heat exchanger/TE device system analyses of sectioned TE system designs have been performed, creating unique efficiency–power maps that provide better understanding and comparisons of design tradeoffs and nominal and off-nominal system performance conditions. New design perspectives and mathematical foundations in optimization of sectioned TE design approaches are discussed that provide insight on how to optimize such sectioned TE systems. System performance analyses using ANSYS® TE modeling capabilities have integrated heat exchanger performance models with ANSYS® TE models to extend its analysis capabilities beyond simple constant hot-side and cold-side temperature conditions. Analysis results portray external resistance effects, matched load conditions, and maximum power versus maximum efficiency points simultaneously, and show that maximum TE power occurs at external resistances slightly greater than the TE module internal resistances in these systems. Mathematical relationships are given providing the foundation for this phenomenon.

Key words: Battery recharging, portable power, LAST/LASTT thermoelectric materials, thermoelectric system analysis

Abbreviations

Variables

N	Number of TE couples
P_T	Total system power (W)
P_i	Power in section i of sectioned design (W)
$Q_{h,i}$	Hot-side heat transfer in section i

(Received June 22, 2012; accepted December 26, 2012; published online February 12, 2013)

R_o External resistance (Ω)
R TE couple internal resistance (Ω)
T Absolute temperature (K)
UA Heat exchanger effective conductance (W/K)
$\dot{m}$ Mass flow rate (kg/s)
C_p Specific heat capacity (J/kg-K)
J Electric current density vector (A/m^2)
ZT Dimensionless figure of merit $ZT = (\alpha^2\sigma/\kappa)T$
ΔT $(T_h - T_c)$ (K)

Greek

ε Heat exchanger effectiveness
η_i Conversion efficiency in section i
η_T Total system efficiency
ρ Density (kg/m^3)
φ Electric scalar potential
κ Thermal conductivity (W/m-K)
$[\lambda]$ Thermal conductivity matrix (W/m-K)
σ Electrical conductivity (S/m)
$[\sigma]$ Electrical conductivity matrix (S/m)
α Seebeck coefficient (V/K)
$[\alpha]$ Seebeck coefficient matrix (V/K)
$[\Pi]$ Peltier coefficient matrix (V)
$[\varepsilon]$ Dielectric permittivity matrix (F/m)

Subscripts

amb Ambient conditions
exh Exhaust flow conditions
h Quantity associated with TE device hot side
c Quantity associated with TE device cold side
1 Section 1 of dual-sectioned TE design
2 Section 2 of dual-sectioned TE design

INTRODUCTION

Waste heat loss represents billions of dollars worldwide in lost capital each year because it provides no useful work to the world economies. Thermoelectric power systems can provide one solution to recover and convert this waste thermal energy to useful electrical output that benefits societies worldwide. As a result there is a tremendous amount of research and development ongoing worldwide to develop TE materials and systems that are high performance and cost effective. The Strategic Environmental Research and Development Program (SERDP) office has recently funded important work that has further developed new lead-antimony-silver-telluride (LAST) and lead-antimony-silver-telluride-tin (LASTT) compounds originally reported by Kanatzidis et al.,[1,2] then designed and fabricated new advanced TE devices based on these LAST/LASTT materials. This SERDP project has also designed and developed new high-performance microchannel heat exchangers, and developed new TE system designs based on new sectioned system design techniques and perspectives. This paper discusses the new system design techniques and perspectives that resulted from this work.

Figures 1 and 2 show the ZT behavior of a variety of thermoelectric (TE) materials that have been researched and developed in the past 10 years.[1–15] Many of the new TE materials have not been taken to a device level that can ultimately create useable power systems. The most recent SERDP progress with LAST and LASTT compounds has transitioned them into high-performance TE devices using a segmented-element design. These recent materials are hot-pressed and sintered (HPS) versions of early LAST/LASTT materials, with much better structural and thermal fatigue characteristics that have enabled TE device design, fabrication, and high-temperature operation. Matchanov et al.[16] and Hendricks et al.[17] presented and discussed the thermoelectric, structural, and thermal fatigue properties of these latest LAST/LASTT materials. These materials have shown high power factors, adequate structural properties (i.e., Young's modulus and Poisson's ratio), and good thermal fatigue characteristics upon thermal cycling.[18]

Past work by Hendricks[19] and Hendricks and Lustbader[20,21] laid the technical foundations for the TE waste heat recovery system design work discussed here. Additional work by Crane and Jackson,[22] LaGrandeur et al.,[23] and Crane and Bell[24] investigated TE system designs for automotive exhaust heat recovery systems, including methods and techniques for dealing with transient thermal conditions in automotive exhaust streams. Crane[25] presented recent results on detailed thermal/thermoelectric performance analysis of automotive waste heat recovery designs and their performance in responding to transient exhaust stream thermal conditions.

Table I presents typical exhaust flow conditions in certain diesel engine/generator applications that were used to design the TEG systems of interest for SERDP applications. They serve as reference cases for the optimization techniques discussed herein. These are typical steady-state exhaust conditions in the applications of interest here.

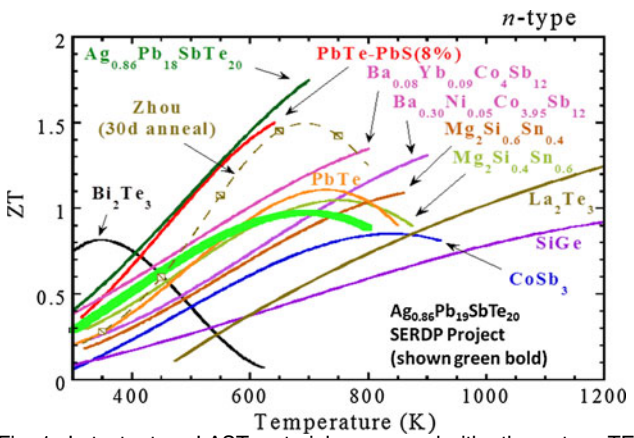

Fig. 1. Latest *n*-type LAST materials compared with other *n*-type TE materials.[1–15,17]

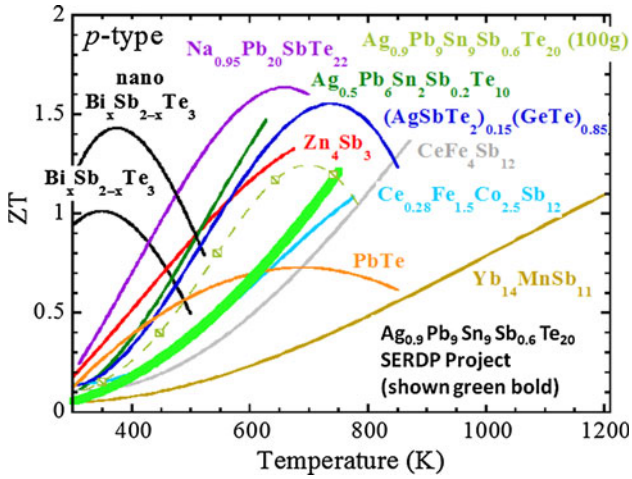

Fig. 2. Latest *p*-type LASTT materials compared with other *p*-type TE materials.[1–15,17]

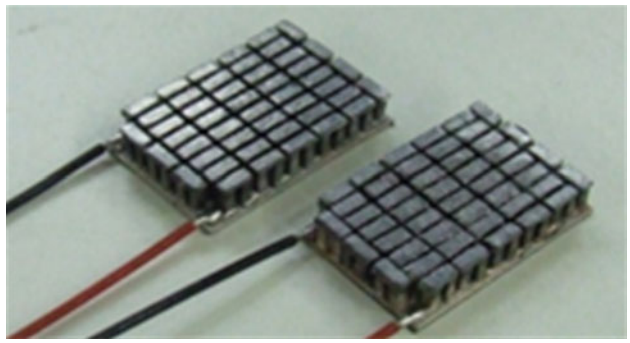

Fig. 3. First operational high-performance TE devices using LAST/LASTT materials in segmented elements.[17]

Table I. Typical exhaust conditions in certain diesel engine/generator applications

	Exhaust Temperature (K)	Mass Flow Rate (kg/s)
30–60-kW diesel engine/generator	754–780	0.1–0.16

LAST/LASTT THERMOELECTRIC DEVICES

Tellurex Corporation transitioned the latest LAST and LASTT materials into the first operating high-performance TE devices that employ segmented *n*-type LAST–bismuth telluride elements and *p*-type LASTT–bismuth telluride elements. These newest LAST and LASTT materials are hot-pressed and sintered materials, which have demonstrated power factors and can be tailored to effectively interface with *p*- and *n*-type bismuth telluride materials. Figure 3 shows these new TE devices, which have been tested successfully at hot-side temperature of T_h = 400°C and cold-side temperature of T_c = 40°C. These modules have demonstrated room-temperature electrical resistances in line with theoretical expectations (3.1 ohms) and efficiencies greater than 7% at these operating temperatures. These modules now need further testing at hot-side temperatures up to 500°C with T_c in the 50°C to 150°C range. Promethient LLC has interests in pursuing this additional high-temperature TE module testing.

THERMOELECTRIC SYSTEM ANALYSIS

Thermoelectric Design Optimization

The temperature differentials are large enough in automotive exhaust streams, diesel engine exhaust streams, and other industrial exhaust streams that sectioned thermoelectric design can be considered and exploited. The system design work in SERDP[17] investigated the design and performance of sectioned system designs and the critical high-performance hot-side microchannel heat exchanger designs developed in the project. The hot exhaust gases in these applications cool off significantly as they pass through the hot-side heat exchangers and dissipate thermal energy into the TE system. Certain sections of the TE system can actually see substantially different exhaust temperatures and thermal transfers along the exhaust flow length, and one optimum design is not sufficient to optimize system performance over the entire exhaust temperature range encountered. The advanced sectioned TE design solves this problem by allowing one to optimize separate, individual TE sections as the exhaust temperature decreases and hot-side thermal transfers vary along the flow length. Figure 4 schematically exemplifies a dual-sectioned TE design concept for a 30-kW diesel generator in this work. The lower half of Fig. 4 shows the TE device designs used in each section. The high-temperature section 1 uses the segmented-element TE device design shown in Fig. 3, which incorporates *n*-type LAST and *p*-type LASTT materials segmented with *n*- and *p*-type bismuth telluride, respectively. The low-temperature section design investigated both segmented-element designs and single-material-element TE device design with just *p*- and *n*-type bismuth telluride in the TE device design. The final design used single-material bismuth telluride TE devices as shown in Fig. 4. This sectioned design produces more output power or operates at higher overall system efficiency than a single-section design producing the same output power because the design allows the TE sections to operate optimally for the exhaust temperatures and hot-side thermal transfers they encounter.

The exhaust flow in this design case enters the first section at 754 K and drops down to 675.5 K as it transfers its thermal energy to the first TE section, at which point it enters the second section and subsequently drops to 591.3 K as it transfers additional thermal energy to the second TE section. The

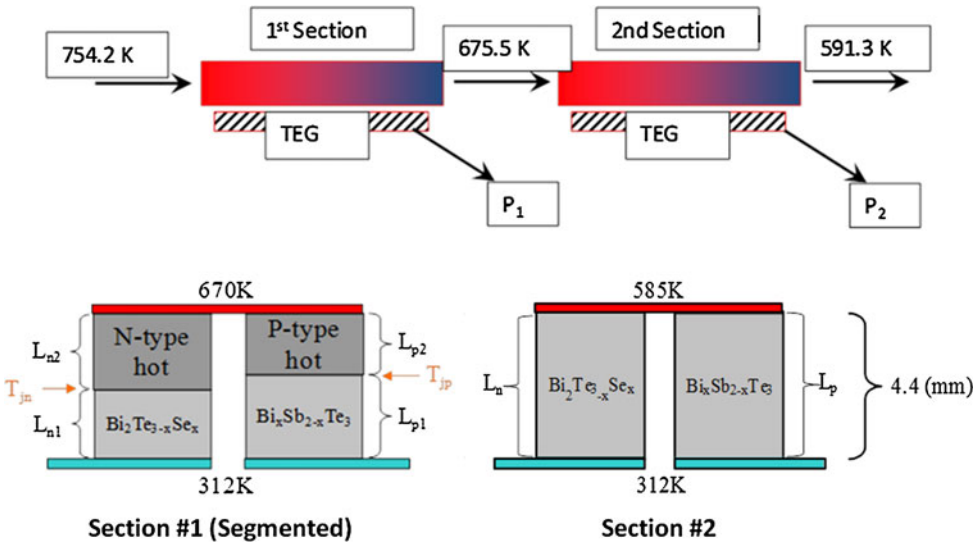

Fig. 4. Schematic diagram of a dual-sectioned TE system design for a typical 30-kW diesel generator.

temperature conditions in these two sections are created by the fundamental performance of the hot-side microchannel heat exchanger designs in these two sections that are characterized by their overall UA_h value and resulting heat exchange effectiveness, ε_h,[26] which accounts for all the convective and conductive thermal transfer pathways and resistances in these heat exchangers. The UA_h of the microchannel heat exchanger designs used in these two sections[17] was estimated using techniques in Kays and London[26] to be approximately 377 W/K, and the effectiveness of these heat exchangers is typically about 0.93. The constant cold-side temperature condition of 312 K is maintained by high-performance water microchannel heat exchangers.[17] These heat exchanger performance values were used in the TE system analyses discussed below.

Figure 5 demonstrates the design optimization analysis results for a typical dual-sectioned design using the techniques described in Hendricks[19] and Hendricks and Lustbader.[20,21] The dual-sectioned or any multisectioned design creates significant design tradeoffs between the power output and efficiency in each section in seeking the optimum overall system performance, whether that is maximum overall system efficiency or maximum system power output. There are two sets of maximum efficiency–power curves in Fig. 5, one for section 1 designs and a second for section 2 designs in Fig. 4. The maximum efficiency–power curves identify the loci of maximum efficiency designs (defined by techniques in Angrist[27] and Cobble[28]) and their resulting power outputs produced by the coupled interaction of the TE device design and the hot-side and cold-side heat exchangers (described in Hendricks[19] and Hendricks and Lustbader[20,21]) in sections 1 and 2. Figure 5 analysis results were performed for T_{exh} = 754 K, T_{amb} = 300 K, and exhaust mass flow rate of ~0.1 kg/s, as shown in the legend, and using segmented LAST/LASTT elements in section 1 and bismuth telluride TE elements in section 2 (as shown in Fig. 4). The TE material properties for the *p*- and *n*-type materials are shown in Figs. 1 and 2. Both sections are assumed to be water-cooled at a water ambient temperature of 300 K.

There is a tremendous amount of design optimization information in Fig. 5 for the two sections of this dual-sectioned design. The section 1 efficiency–power curves show the various maximum efficiency–power points for several different hot-side and cold-side temperature combinations ($T_{h,1}$, $T_{c,1}$) resulting from the coupled interaction between the TE device design and hot-side heat exchanger design characterized by UA_h = 377 W/K. Although there is necessarily a different TE couple number and *p*- and *n*-type TE area at each design point on the curve, these curves show the range and domain of possible efficiency and power combinations possible in section 1. The hot-side heat exchanger design and the TE performance at each $T_{h,1}$ along the section 1 efficiency–power curves then create a unique entrance exhaust temperature input to section 2 shown in Fig. 4. This situation then creates a family of maximum efficiency–power curves for the section 2 design, one for each of the section 1 $T_{h,1}$ conditions along the section 1 curves. Figure 5 shows four such section 2 design curves corresponding to four design points on the section 1 curve for a cold-side temperature condition of 312 K. What is clear is that, as the section 1 design changes efficiency and power output, and therefore impacts the input exhaust temperature for section 2, there is a uniquely defined section 2 efficiency–power curve that dictates its efficiency–power characteristics resulting from the coupled interaction of the TE device

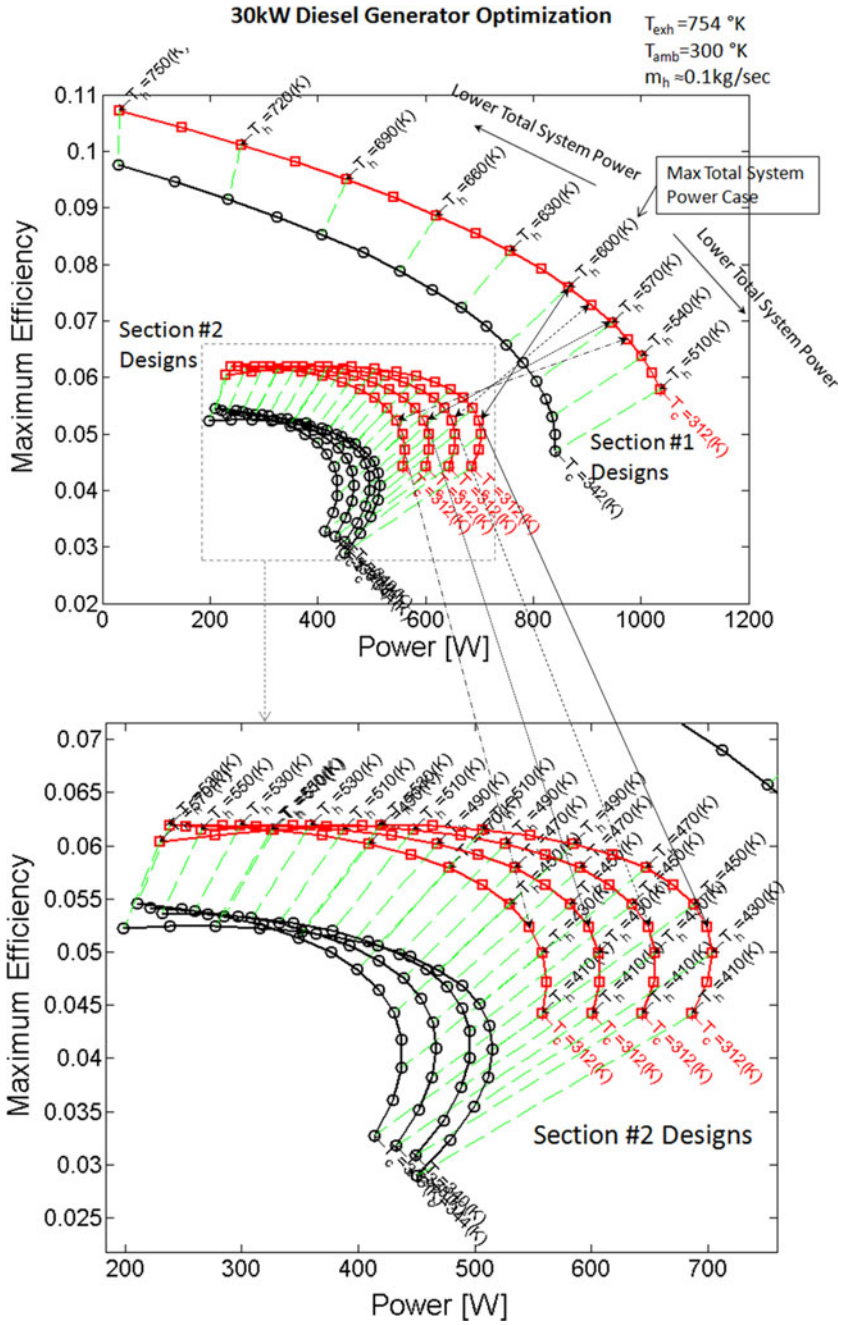

Fig. 5. Dual-sectioned maximum efficiency–power maps defining loci of maximum efficiency designs in sections 1 and 2.

designs and the hot-side heat exchanger design in section 2. The four section 1 points selected for $T_{c,1}$ = 312 K demonstrate that, as the section 1 power decreases and its efficiency increases, the section 2 power output generally increases while the section 2 efficiency stays roughly the same in a range around 5.5% to 6.2%. This section 2 efficiency is largely governed by the TE material properties of the bismuth telluride materials in section 2. Different section 2 TE materials and properties would show somewhat different efficiency–power behavior and sensitivities.

This behavior and the interaction between sections 1 and 2 creates a maximum total system power point because the section 2 increases in power only offset or override the section 1 decreases in power up to a point. The maximum total system power point does not reside even close to the maximum point for section 1 as shown in Fig. 5. Understanding this design power tradeoff and knowing where the maximum total system power point resides is critical to designing a dual-sectioned system to satisfy any given efficiency–power requirement, whether it be dictated by maximum

efficiency concerns or maximum power concerns. This behavior and interaction between section 1 and 2 designs can occur in general at any common cold-side temperature ($T_{c,1}$ and $T_{c,2}$) conditions as shown in Fig. 5. This behavior and interaction will also occur in general for any combination of TE materials in sections 1 and 2. In both of these cases the maximum total power point may shift around as a result of the impact of TE material performance or cold-side temperature effects on power output, and it is crucial to quantify this shift if it occurs.

Figure 5 also demonstrates the impact of cold-side temperature selection on the optimum performance designs. Both the maximum efficiency and power output decrease as expected when the cold-side temperature increases. In this case the performance decline was found to be quite significant. The benefit of this maximum efficiency–power map is that it quantifies the cold-side temperature impact directly on this one performance map.

One may be interested in a quite common design question of selecting the proper section 1 and 2 hot-side temperatures, $T_{h,1}$ and $T_{h,2}$, to maximize the system power output from this dual-section design given that other design parameters, such as cold-side temperatures, are held constant. One could then predict approximately where to operate on the maximum efficiency–power curves in Fig. 5 to satisfy that condition. The total power given by

$$P_T(T_{h,1}, T_{h,2}) = P_1 + P_2 = \eta_1 \cdot Q_{h,1} + \eta_2 \cdot Q_{h,2} \quad (1)$$

must be maximized, where the total power, P_T, is a function of $T_{h,1}$ and $T_{h,2}$. TE material properties being functions of temperature are also a function of these two temperatures. P_T would maximize in a dual-section design when the following two conditions are satisfied simultaneously:

$$\left(\frac{\partial P_T}{\partial T_{h,1}}\right) = 0, \quad (2)$$

$$\left(\frac{\partial P_T}{\partial T_{h,2}}\right) = 0. \quad (3)$$

This would mandate that

$$\eta_1 \cdot \frac{\partial Q_{h,1}}{\partial T_{h,1}} + Q_{h,1} \cdot \frac{\partial \eta_1}{\partial T_{h,1}} + \eta_2 \cdot \frac{\partial Q_{h,2}}{\partial T_{h,1}} = 0, \quad (4)$$

$$\eta_2 \cdot \frac{\partial Q_{h,2}}{\partial T_{h,2}} + Q_{h,2} \cdot \frac{\partial \eta_2}{\partial T_{h,2}} = 0. \quad (5)$$

The third term in Eq. 4 explicitly demonstrates the mathematical interdependence between the two section designs and its impact on optimizing the overall power output. Equation (4) can be reformulated by realizing that

$$\frac{\partial Q_{h,2}}{\partial T_{h,1}} = \frac{\partial Q_{h,2}}{\partial T_{exh,2}} \cdot \frac{\partial T_{exh,2}}{\partial T_{h,1}} = \frac{\partial Q_{h,2}}{\partial T_{exh,2}} \cdot \varepsilon_{h,1}, \quad (6)$$

where $\varepsilon_{h,1}$ is the effectiveness of the hot-side heat exchanger in section 1. Equation (4) then clearly demonstrates mathematically that the upstream section 1 design impacts the optimization choices one makes in the downstream section 2 of a dual-section design. The same type of upstream relationship would occur and impact downstream optimization choices in any multisectioned design.

The simultaneous relationships depicted in Eqs. (2) and (3) provide the necessary conditions to determine the optimum choice of $T_{h,1}$ and $T_{h,2}$ in Fig. 5 for maximizing power output. The design optimization analyses described by Hendricks,[19] Hendricks and Lustbader,[20,21] Angrist,[27] and Cobble[28] provide the necessary equations to evaluate the various derivatives shown in Eqs. (2–6) and establish the resulting simultaneous optimization equations to maximize P_T (Eq. 1) for the dual-sectioned system shown in Fig. 4. This technique was utilized to predict the $T_{h,1}$ and $T_{h,2}$ for the sectioned design shown in Fig. 4 utilizing the LAST and LASTT and bismuth telluride p- and n-type properties shown in Figs. 1 and 2. This technique determined that the maximum total system power output of this segmented, sectioned design occurred at optimum hot-side temperatures of $T_{h,1}$ = 615 K and $T_{h,2}$ = 465 K. The predicted maximum power output using this technique and accounting for thermal losses was approximately 1560 W. Figure 5 shows that, upon performing the system design optimization analysis across the entire potential design domain, using the techniques described by Angrist,[27] Cobble,[28] Hendricks,[19] and Hendricks and Lustbader[20,21] for the two sections, the maximum power conditions were achieved at optimum hot-side temperatures of $T_{h,1}$ = 600 K and $T_{h,2}$ = 440 K as shown in Fig. 5. The maximum power condition from that complete design domain analysis was 1565 W. This shows reasonable agreement between the two design optimization techniques given the challenges of modeling segmented TE elements, and demonstrates this new technique for determining the optimum section hot-side temperatures that maximize the total system power output before running the complete design domain analysis shown in Fig. 5. It also provides a second powerful analysis technique for utilizing and assessing the results and design tradeoffs in Fig. 5, and a solid reference point identifying the maximum total system power design relative to all possible system designs within the complete design domain. This allows one to make intelligent design choices when trading off one sectioned system design and system efficiency–power combination versus another.

A multisectioned design having more than two sections would have a similar set of simultaneous differential equations for each stage i, i.e.,

$$\left[\left(\frac{\partial P_T}{\partial T_{h,i}}\right) = 0\right]_i, \tag{7}$$

which could be solved for each $T_{h,i}$ in the multisectioned system to maximize power. If $T_{h,i}$ is considered an i-element vector, then the Eq. (7) condition is equivalent to $(\nabla_T P_T) = 0$. This optimization analysis process was demonstrated for the dual-sectioned system in Fig. 4 and the dual-sectioned analysis results shown in Fig. 5 as an example of the technique.

A second common design question of interest is selecting the proper section 1 and 2 hot-side temperatures, $T_{h,1}$ and $T_{h,2}$, to maximize the overall system efficiency from this dual-section design given that other design parameters, such as cold-side temperatures, are held constant. One would then be able to predict approximately where to operate on the maximum efficiency–power curves in Fig. 5 to satisfy that condition. The overall system efficiency is given by

$$\eta_T(T_{h,1}, T_{h,2}) = \frac{P_1 + P_2}{Q_{h,1} + Q_{h,2}} = \left(\frac{\eta_1 \cdot Q_{h,1} + \eta_2 \cdot Q_{h,2}}{Q_{h,1} + Q_{h,2}}\right). \tag{8}$$

In this case the total system efficiency, η_T, which is a function of $T_{h,1}$ and $T_{h,2}$, must be maximized, accounting for the temperature-dependent TE material properties. η_T would maximize in a dual-section design when the following two conditions are satisfied simultaneously:

$$\left(\frac{\partial \eta_T}{\partial T_{h,1}}\right) = 0, \tag{9}$$

$$\left(\frac{\partial \eta_T}{\partial T_{h,2}}\right) = 0. \tag{10}$$

This would result in the following two conditions:

$$\begin{aligned}\left(\frac{1.0}{Q_{h,1} + Q_{h,2}}\right) \cdot \left(Q_{h,1} \cdot \frac{\partial \eta_1}{\partial T_{h,1}} + \eta_1 \cdot \frac{\partial Q_{h,1}}{\partial T_{h,1}}\right. \\ \left. + \eta_2 \cdot \varepsilon_{h,1} \cdot \frac{\partial Q_{h,2}}{\partial T_{exh,2}}\right) - \left(\frac{\eta_1 \cdot Q_{h,1} + \eta_2 \cdot Q_{h,2}}{(Q_{h,1} + Q_{h,2})^2}\right) \\ \cdot \left(\frac{\partial Q_{h,1}}{\partial T_{h,1}} + \varepsilon_{h,1} \cdot \frac{\partial Q_{h,2}}{\partial T_{exh,2}}\right) = 0,\end{aligned} \tag{11}$$

$$\begin{aligned}\left(\frac{1.0}{Q_{h,1} + Q_{h,2}}\right) \cdot \left(Q_{h,2} \cdot \frac{\partial \eta_2}{\partial T_{H,2}} + \eta_2 \cdot \frac{\partial Q_{h,2}}{\partial T_{h,2}}\right) \\ - \left(\frac{\eta_1 \cdot Q_{h,1} + \eta_2 \cdot Q_{h,2}}{(Q_{h,1} + Q_{h,2})^2}\right) \cdot \left(\frac{\partial Q_{h,2}}{\partial T_{h,2}}\right) = 0.\end{aligned} \tag{12}$$

Equation (6) has been incorporated into the proper terms where appropriate in Eq. (11). Once again, these terms in Eq. (11) clearly demonstrate the mathematical interdependence between the two section designs and its impact on optimizing the overall total efficiency. Just as in the power maximization case above, Eq. (11) clearly demonstrates mathematically that the design of upstream section 1 can impact the optimization choices possible in the downstream section 2 design in a dual-section design. Once again, as in power optimization, the same type of upstream–downstream interdependence would occur, and the upstream design impacts the downstream optimization choices in any multisectioned design. These relationships quantify this intuitive connection between the two sections.

The simultaneous relationships depicted in Eqs. (11) and (12) provide the necessary conditions to determine the optimum choice of $T_{h,1}$ and $T_{h,2}$ in Fig. 5 for maximizing the total system efficiency. The design optimization analyses described by Hendricks,[19] Hendricks and Lustbader,[20,21] Angrist,[27] and Cobble[28] provide the necessary equations to evaluate the various derivatives shown in Eqs. (9–12) and establish the resulting simultaneous optimization equations to maximize η_T (Eq. 8) for the dual-sectioned system shown in Fig. 4. Solution of Eqs. (11) and (12) creates designs which necessarily have higher hot-side temperatures, $T_{h,1}$ and $T_{h,2}$, than in the power maximization case described above. This creates optimum η_T system designs at higher efficiency/lower power points on curves in Fig. 5. Lower power conditions than in power maximization are created because lower hot-side heat transfers necessarily result from the higher hot-side temperatures when considering constant exhaust flow temperatures in this analysis.

A multisectioned design having more than two sections would have a similar set of simultaneous differential equations:

$$\left[\left(\frac{\partial \eta_T}{\partial T_{h,i}}\right) = 0\right]_i \tag{13}$$

for each ith section, which could be solved for each $T_{h,i}$ in the multisectioned system to maximize η_T. If $T_{h,i}$ is considered an i-element vector, then the Eq. (13) condition is equivalent to $(\nabla_T \eta_T) = 0$. This process and the similar process in multisection power maximization is how one would use the results in Fig. 5 to determine which optimum design point or points to target depending on any given set of requirements in a given design application. They provide valuable reference points in intelligently deciding which overall design point is best when considering all the system design requirements and, more importantly, which design compromises are appropriate in any given sectioned TE design.

SERDP had ambitious system design objectives to design a TE generator producing 1600 W at near 10% conversion efficiency from the waste exhaust heat in diesel generators, incinerators, and mobile kitchen units. The design optimization results in

Fig. 5 for a 30-kW diesel engine/generator demonstrated clearly that this goal could not be achieved using the available thermal energy and thermal conditions in a 30-kW diesel generator and the LAST and LASTT TE materials and modules in Figs. 1–3. The reasons for this were primarily that the TE material properties were not quite good enough and the amount of thermal energy available in the 30-kW diesel generator exhaust flow and transferable to the TE device hot sides was not high enough. This demonstrates the key benefit of the TE design optimization techniques and approach shown in Fig. 5. They quickly determine and highlight the potential efficiency–power performance possible in various optimum TE designs in a given application and provide immediate design guidance in achieving the design goals and requirements in a given waste heat recovery application.

As a result of these analysis techniques, an alternate diesel generator and optimum TE design configuration were identified using a 60-kW diesel generator that could come much closer to meeting the design requirements of this application. Additional system optimization analyses similar to those shown in Fig. 5 were then performed for this 60-kW diesel generator configuration. A new optimum system design using the new LAST and LASTT TE materials and modules in Figs. 1–3 was identified that could get much closer to the performance goals, and both single- and dual-section optimum TE system designs were identified that provided enhanced performance flexibility. The single-section optimum TE design for the 60-kW case could produce nearly 1600 W at about 9.8% conversion efficiency, while a dual-section optimum TE design could produce about 2700 W at about 8.5% conversion efficiency. The single-section optimum TE design was carried forward to TE system performance analysis because it could satisfy the design goals with less cost and complexity.

It should be noted that the design optimization techniques presented here allowed one to identify useful, flexible, and robust waste heat recovery designs for both 30-kW and 60-kW diesel generator configurations in SERDP. These designs provide several useful and flexible waste heat recovery design options applicable to diesel generators and incinerators in military and commercial applications, and they quantify the potential efficiency–power performance using the LAST and LASTT materials and modules in Figs. 1–3.

Thermoelectric System Performance Analysis

Thermoelectric system performance analysis, with simultaneously coupled heat exchanger and TE device performance, was carried out on the selected single-section optimum TE system design for the 60-kW diesel generator configuration using the LAST, LASTT, and bismuth telluride materials shown in Figs. 1 and 2 and the segmented-element TE module design shown in Fig. 3. The system design performance analysis was conducted at 100% and 75% of full diesel generator power, where the exhaust flow temperature conditions were 780 K and 733 K, respectively, and the exhaust mass flow was a constant 0.16 kg/s. The finite-element software ANSYS® version 12.0 was used to conduct the system-level TE performance analysis.[29,30]

Heat exchanger performance was modeled using the effectiveness-NTU thermal analysis techniques in Kays and London.[26] The heat transfer from the hot-side exchanger was given by

$$Q_{\mathrm{h}} = \varepsilon_{\mathrm{h}} \times \dot{m}_{\mathrm{h}} \times C_{\mathrm{p,h}} \times (T_{\mathrm{exh}} - T_{\mathrm{h}}), \qquad (14)$$

where ε_{h} is the hot-side exchanger effectiveness, given by

$$\varepsilon_{\mathrm{h}} = 1 - \mathrm{e}^{\frac{-UA_{\mathrm{h}}}{\dot{m}_{\mathrm{h}} C_{\mathrm{p,h}}}}.$$

Similarly, the heat carried away by the coolant in the cold-side exchanger is calculated as

$$Q_{\mathrm{c}} = \varepsilon_{\mathrm{c}} \times \dot{m}_{\mathrm{c}} \times C_{\mathrm{p,c}} \times (T_{\mathrm{amb}} - T_{\mathrm{c}}), \qquad (15)$$

where ε_{c} is the cold-side exchanger effectiveness, given by

$$\varepsilon_{\mathrm{c}} = 1 - \mathrm{e}^{\frac{-UA_{\mathrm{c}}}{\dot{m}_{\mathrm{c}} C_{\mathrm{p,c}}}}.$$

The thermoelectric system performance analysis integrated and coupled the thermal transfer Eqs. (14) and (15) with the ANSYS® TE system analysis described below for a range of external resistances, R_{o}. Interfacial energy balances dictated by Eqs. (14) and (15) were incorporated into the ANSYS® TE model at the hot and cold sides of the TE device. The hot- and cold-side temperatures T_{h} and T_{c} were determined to equate the TE device hot-side and cold-side thermal transfer requirements, determined by the ANSYS® TE model, with the heat transfers from and to the hot- and cold-side heat exchangers, respectively. In this manner, the integrated effect of the hot-side and cold-side heat exchanger performance was accounted for in the ANSYS® TE system-level performance analysis. Because the TE device current, I, is dependent on R_{o}, the analysis was repeated for different values of R_{o} and the vectors of T_{h} and T_{c} were obtained for the range of R_{o} investigated. The TE element temperature distributions; heat flows; current densities; and TE module and system efficiency, voltage, current, and power output vectors were then determined from the T_{h} and T_{c} vectors for the range of R_{o}. This ANSYS®-based TE system analysis could therefore predict the performance of a given system at nominal and off-nominal conditions as the external resistance is changed, thereby causing the voltage/current output to change in response to the varying

resistance conditions. This unique integrated TE system analysis technique, using the ANSYS® TE modeling capability, couples a prescribed heat exchanger performance condition at the ANSYS® TE model hot-side and cold-side boundaries, allowing one to extend the ANSYS® TE modeling capability while working within the confines of its analysis structure.

Equations (16) and (17) are the governing equations that ANSYS® uses to solve for the thermoelectric behavior and performance in the TE module.[29] These equations are formed by coupling the heat flow and electric charge continuity equations with a set of thermoelectric constitutive equations:[30]

$$\rho C\frac{\partial T}{\partial t}+\nabla.([\Pi].\boldsymbol{J})-\nabla.([\lambda].\nabla T)=\dot{q}, \tag{16}$$

$$\nabla.\left([\varepsilon].\nabla\frac{\partial\varphi}{\partial t}\right)+-\nabla.([\sigma].[\alpha].\nabla T)+\nabla.([\sigma].\nabla\varphi)=0. \tag{17}$$

One of the advantages of using ANSYS® is that the temperature-dependent TE material properties such as the Seebeck coefficient, electrical conductivity (or resistivity), and thermal conductivity are evaluated at specific temperatures throughout the elements. Hence, the predicted TE conversion efficiency, power output, and thermal transport calculations accurately represent and reflect the temperature, current, and voltage conditions within the TE couples and module.

This ANSYS® analysis was performed for the selected 47-couple TE module design (Fig. 3) within the single-section TE generator system. Figure 6 illustrates the finite-element model of the SERDP TEG module. The module consists of 47 couples with 1.4 mm × 1.4 mm × 4.4 mm segmented TE elements. The couples are connected in series using copper tabs and are attached to an alumina substrate. A circuit element with known resistance (not shown in Fig. 6) is connected between the end of the first and last (47th) TE couple. This resistance element is required to calculate the power output

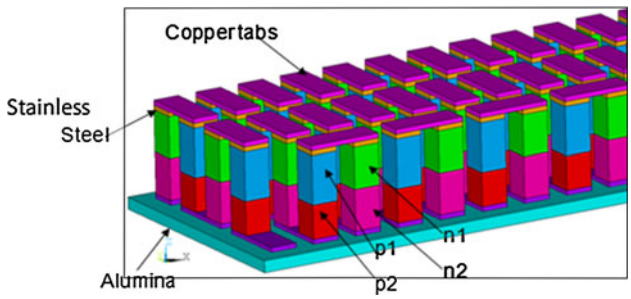

Fig. 6. Finite-element model of the TEG module.

from the module in ANSYS®. The temperature-dependent material property curves for the Seebeck coefficient α, the electrical conductivity σ, and the thermal conductivity κ were input to the FE model. The model was solved for the static thermal distribution with hot- and cold-side temperatures as boundary conditions that were obtained previously using techniques described above, establishing interfacial heat balances at the heat exchanger interfaces with the ANSYS® TE model. Figure 7 shows a case of the temperature distribution in the TE module for T_{exh} = 780 K and T_{amb} = 300 K [$(R_o/R_{\text{int}},\ \Delta T)$ = (2.13, 355) point in Fig. 9]. The contact resistance is included in the finite-element model by adding 10% of the couple's total internal resistance to the resistance of the copper tab connecting these couples.

Figure 8 demonstrates the TE module power dependency on the external load resistance on a per-module basis resulting from the system-level analysis at 100% and 75% of full diesel generator power conditions. The peak module power condition occurs and is shown, but the power versus resistance behavior does not follow the familiar parabolic power profile for the TE power modules operating with constant temperature differentials. The reason for this is that this type of system-level performance analysis does not create a constant temperature differential across the TE module as the external load resistance increases for constant exhaust temperature conditions. The temperature differential across the TE module actually increases as the external resistance increases, thereby creating the unique power–resistance profile shown in Fig. 8. Actual tests on different TE waste heat recovery systems at the Pacific Northwest National Laboratory have confirmed that this power versus electrical load resistance profile is correct and occurs in exhaust energy recovery systems with constant exhaust temperature conditions.

The varying temperature differential across the TE module creates an important effect demonstrated in the power data of Figs. 8 and 9; That is, the peak power point does not occur at the traditional $R_o = N \times R$ condition ($N \times R$ = TE module resistance, R_o = external resistance). Instead, it occurs at $R_o > N \times R$ in the data shown in Figs. 8 and 9. When considering the power output from the TE modules, given by

$$P=\frac{(N\times\alpha.\Delta T)^2}{(N\times R+R_0)^2}\cdot R_0, \tag{18}$$

The traditional $R_o = N \times R$ peak power condition occurs when this equation is differentiated and set to zero assuming ΔT is constant. However, to determine the peak power condition in this system-level analysis, ΔT must be assumed variable and the differentiation then becomes more complex. The peak power condition then becomes

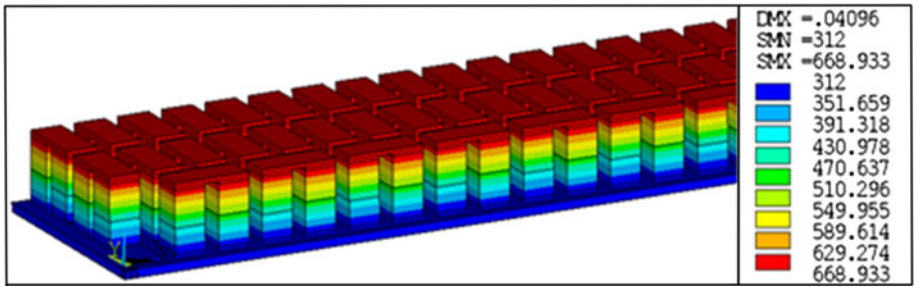

Fig. 7. Temperature distribution in the module with $T_h \approx 669$ K and $T_c = 312$ K (temperatures in K).

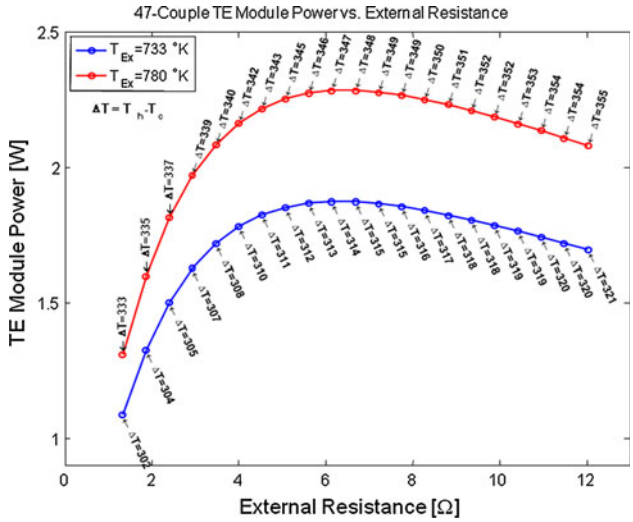

Fig. 8. Electrical resistance effect on module power.

$$R_0 = (N \cdot R) + \frac{(2 \cdot R_0 \cdot N \cdot R + 2 \cdot R_0^2)}{\Delta T} \cdot \frac{\partial(\Delta T)}{\partial R_0}. \quad (19)$$

This equation shows that $R_o > N \times R$ by an amount related to the derivative of the module temperature differential with respect to R_o, and additional terms related to the module temperature differential itself and R_o. This equation results in a quadratic relationship for R_o that explicitly quantifies the $R_o > N \times R$ peak power condition in any particular system-level analysis. It accurately predicts the peak power resistance value shown in the TE module power predictions in Fig. 8 derived from our system-level performance analysis.

Figure 9 shows the projected TE module efficiency–system power maps resulting from system-level analysis of the full single-section TEG design in a 60-kW diesel generator configuration at 100% of full power (T_{exh} = 780 K) and 75% of full power output (T_{exh} = 733 K) based on the ANSYS® TE/heat exchanger model analyses discussed above. The full TEG system included approximately 640 of the 47-couple TE modules. The ambient cooling temperature was set at 300 K in these analyses. Figure 9 presents a unique method of exhibiting the system analysis results in TE module efficiency–system power maps, with the efficiency–power mapping simultaneously displaying the (external load/internal resistance) ratios and module temperature differentials on the performance mapping. The properties of the *p*- and *n*-type TE materials vary with temperature, and thus with the location and segmentation along the TE elements, and the internal resistance also depends on the electrical contact materials and connections within the TE module. Therefore, the calculation of the total internal module resistance is not straightforward. In order to calculate the internal resistance in the ANSYS® TE module model, an intermediate calculation was performed whereby the external resistance is varied to get the power versus external resistance curve for constant hot- and cold-side temperature conditions at each (T_h, T_c) combination considered in the system analysis. Under constant hot- and cold-side temperature conditions, the power versus resistance curve peaks at the matching load resistance. The value of this resistance at the peak power in this intermediate constant-temperature analysis represents the module total internal resistance for those (T_h, T_c) conditions in the full system analysis. This method is repeated to get the internal resistance, R_{int}, and then the (R_{ext}/R_{int}) of the module for each of the module efficiency–power points in Fig. 9. This was again a method used in adapting and utilizing the ANSYS® TE modeling capabilities in the constant exhaust temperature analyses performed here.

The module efficiency–system power map demonstrates the crucial tradeoff between module efficiency and system power output as the external load resistance increases for 100% and 75% of full generator power conditions. An important characteristic in this type of system-level analysis is that increasing the external load resistance simultaneously increases the temperature differential across the TE modules for constant exhaust temperature and ambient cooling temperature conditions. This creates the common behavior that the system power output peaks at a certain critical external load resistance, which is clearly depicted in Fig. 9. This also produces a maximum electrical conversion efficiency at a second, higher critical external load resistance, which is clearly shown in Fig. 9. Both of these key

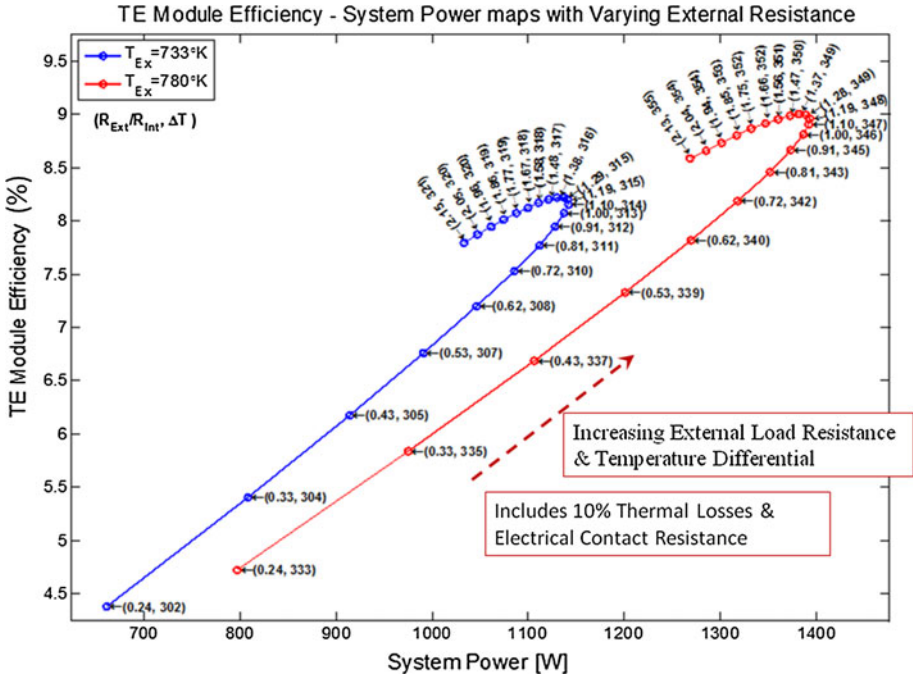

Fig. 9. TEG system power–TE module efficiency tradeoff using LAST/LASTT segmented TE module designs (segmented with bismuth telluride, T_{Ex} = exhaust temperature, conditions noted in legend).

performance conditions are the result of the tradeoff effects of higher temperature differentials across the TE modules producing higher voltage and higher external electrical resistance, decreasing the current. Figure 9 shows that the maximum power output for 100% of full generator power conditions is projected to be about 1.4 kW at just below 9.0% TE module conversion efficiency. The TE module maximum conversion efficiency occurs at about 9% with only a slight decrease in system power to about 1.38 kW. Therefore, the maximum system power point is not far from the maximum system efficiency point in the total TE system performance domain. At 75% full diesel generator power conditions, it is clear that the maximum system power output decreases to about 1.14 kW at about 8.15% module efficiency and the maximum module efficiency occurs near 8.2%, with the system power staying nearly the same at 1.14 kW. This characteristic module-system behavior in Fig. 9 provides useful comparisons of critical operating points in TEG designs.

CONCLUSIONS

Recent work with the Strategic Environmental Research and Development Program office has investigated new thermoelectric (TE) materials and systems that can operate at higher performance levels and show a viable pathway to lightweight, compact, advanced thermoelectric generator systems to recover waste heat from various waste heat sources or combustion-driven systems. New TE materials include nanocomposite materials such as LAST and LASTT compounds. New higher-performance TE devices segmenting LAST/LASTT materials with bismuth telluride have been designed and fabricated. These new TE devices have been tested successfully at hot-side temperature of 400°C and cold-side temperature of 40°C, and they have demonstrated room-temperature electrical resistances in line with theoretical expectations with efficiencies greater than 7%. These new materials and devices have led to unique sectioned TE system designs and new perspectives in sectioned efficiency–power optimization analysis techniques to quickly evaluate a wide variety of total system designs throughout the complete system design space. New techniques and mathematical formalism have also been developed to identify the total system maximum power and maximum efficiency points in the overall design space that can be used with the sectioned efficiency–power optimization maps to establish key system-level design tradeoffs and sensitivities referenced to these optimum points. This new mathematical formalism demonstrates the heat exchanger/TE device interdependencies in the design optimization process. New design performance analysis techniques have also been developed using ANSYS® version 12.0 TE analysis capabilities that allow one to integrate hot-side and cold-side heat exchanger performance by imposing interfacial energy balances into the ANSYS® analysis structure. This allows extension of the ANSYS® version 12.0 capabilities while working within its analysis structure. New analysis perspectives from the ANSYS® TE analysis results have demonstrated unique TE module efficiency–power maps that provide useful performance comparisons of nominal and off-nominal performance conditions

as external load resistance conditions vary. Unique analysis perspectives demonstrate why the maximum power in these TEGs may occur at conditions different from the typical matched load resistance criterion often associated with maximum power. These analysis techniques and results have identified several flexible waste heat recovery system designs based on the new LAST and LASTT materials. The TE modules developed in this work are applicable to the common exhaust temperatures of diesel generators and incinerators in military and commercial applications. Design optimization analyses have quantified the potential efficiency–power performance using these latest LAST and LASTT TE materials and modules for common diesel generator exhaust conditions.

ACKNOWLEDGEMENTS

The authors would like to thank Dr. John Hall, SERDP Sustainable Infrastructure Program Manager, and Carrie Wood, Technical Monitor for their support of this work. The authors also acknowledge and thank the Office of Naval Research for their early research and development in LAST and LASTT thermoelectric materials that provided the foundation for this work.

REFERENCES

1. K.-F. Hsu, S. Loo, F. Guo, W. Chen, J.S. Dyck, C. Uher, T. Hogan, E.K. Pobchroniadis, and M.G. Kanatzidis, *Science* 303, 818 (2004).
2. T.M. Tritt and M.A. Subramanian, *Mater. Res. Soc. Bull.* 31, 188 (2006).
3. Z.H. Dughaish, *Phys. B* 322, 205 (2002).
4. S.R. Brown, S.M. Kauzlarich, F. Gascoin, and G.J. Snyder, *Chem. Mater.* 18, 1873 (2006).
5. T. Caillat, J.-P. Fleurial, and A. Borshchevsky, *J. Phys. Chem. Solids* 58, 1119 (1997).
6. E.A. Skrabek and D.S. Trimmer, *CRC Handbook of Thermoelectrics, Chap. 22*, ed. D.M. Rowe (Boca Raton, FL: CRC, 1995).
7. P.F.P. Poudeu, J. D'Angelo, A. Downey, J.L. Short, T.P. Hogan, and M.G. Kanatzidis, *Angew. Chem. Int. Ed.* 45, 3835–3839 (2006).
8. B. Poudel, Q. Hao, Y. Ma, Y. Lan, A. Minnich, B. Yu, X. Yan, D. Wang, A. Muto, D. Vashaee, X. Chen, J. Liu, M.S. Dresselhaus, G. Chen, and Z. Ren, *Science* 320, 634 (2008).
9. J. Androulakis, K.-F. Hsu, R. Pcionek, H. Kong, C. Uher, J.J. D'Angelo, A. Downey, T. Hogan, and M.G. Kanatzidis, *Adv. Mater.* 18, 1170 (2006).
10. Y. Gelbstein, Z. Dashevsky, and M.P. Dariel, *Phys. B* 363, 196 (2005).
11. M. Zhou, J.-F. Li, and T. Kita, *J. Am. Chem. Soc.* 130, 4527 (2008).
12. X. Shi, H. Kong, C.-P. Li, C. Uher, J. Yang, J. R. Salvador, H. Wang, L. Chen, and W. Zhang, *Appl. Phys. Lett.*, 92, article #182101 (2008).
13. J. Androulakis, C.-H. Lin, H.-J. Kong, C. Uher, C.-I. Wu, T. Hogan, B.A. Cook, T. Caillat, K.M. Paraskevopoulos, and M.G. Kanatzidis, *J. Am. Chem. Soc.* 129, 9780 (2007).
14. X. Tang, Q. Zhang, L. Chen, T. Goto, and T. Hirai, *J. Appl. Phys.* 97, 093712-1 (2005).
15. T. He, J. Chen, H.D. Rosenfeld, and M.A. Subramanian, *Chem. Mater.*, 18 (759) (2006).
16. N. Matchanov, J.D'Angelo, C.-I. Wu, T.P. Hogan, J. Barnard, C.J. Cauchy, T.J.Hendricks, J. Sootsman, and M.G. Kanatzidis, *Proc. Mater. Res. Soc. Fall Meeting,* Boston, MA (2009).
17. T.J. Hendricks, N.K. Karri, T.P. Hogan, J.D'Angelo, C.-I. Wu, E.D. Case, F. Ren, A.Q. Morrison, and C.J. Cauchy, *Energy Harvesting–From Fundamentals to Devices*, edited by H. Radousky, J. Holbery, L. Lewis, F. Schmidt (Mater. Res. Soc. Symp. Proc. 1218E, Warrendale, PA, 2010), Paper ID # 1218-Z07-02. (*Proc. Mater. Res. Soc. 2009 Fall Meeting*, *Symp. Z*, Paper ID # 1218-Z07-02, Boston, MA, 2009).
18. A.Q. Morrison, F. Ren, E.D. Case, D.C. Kleinow, T.J. Hendricks, C.J. Cauchy, and J. Barnard, *Technical Presentation, Materials Science and Technology Conference*, Pittsburgh (2009).
19. T.J. Hendricks, *J Energy Resour.-ASME,* 129, (3), American Society of Mechanical Engineers, New York, pp. 223–231 (2007).
20. T.J. Hendricks and J.A. Lustbader, *Proc. 21st Int. Conf. on Thermoelectrics,* Long Beach, CA, IEEE Catalogue #02TH8657, pp. 381–386 (2002).
21. T.J. Hendricks and J.A Lustbader, *Proc. 21st Int. Conf. on Thermoelectrics,* Long Beach, CA, IEEE Catalogue #02TH8657, pp. 387–394 (2002).
22. D.T. Crane and G.S. Jackson, *Proc. 37th Intersoc. Energy Conversion Eng. Conf.,* IECEC Paper #20076 (2002).
23. J. LaGrandeur, D. Crane, S. Hung, B. Mazar, and A. Eder, *Proc. 25th Int. Conf. on Thermoelectrics*, Vienna, IEEE Catalogue #06TH8931C, pp. 343–348 (2006).
24. D.T. Crane and L.E. Bell, *Proc. ASME Energy Sustainability 2007 Conf.*, Paper #ES2007-36210, Long Beach, CA, (2007).
25. D.T. Crane, *J. Electron. Mater.* 40, 561 (2011).
26. W.M. Kays and A.L. London, *Compact Heat Exchangers*, 3rd ed. (New York: McGraw-Hill, 1984).
27. S.W. Angrist, *Direct Energy Conversion*, 4th ed. (Boston, MA: Allyn and Bacon, 1982).
28. M.H. Cobble, *CRC Handbook of Thermoelectrics, Chap. 39*, ed. D.M. Rowe (Boca Raton, FL: CRC, 1995).
29. ANSYS release 12.0.1 documentation—theory reference, ANSYS, Inc., www.ansys.com, ansysinfo@ansys.com, (2009).
30. E.E. Antonova and D.C. Looman, *Proc. 24th Int. Conf. on Thermoelectrics*, pp. 215–218, (2005).